Octahedral distortions in SrNbO₃: Unraveling the structure-property relation

Victor Rosendal [1,*] Walber H. Brito [2] Milan Radovic,[3] Alla Chikina [3] Mads Brandbyge [4]
Nini Pryds [1,†] and Dirch H. Petersen [1]

¹*Department of Energy Conversion and Storage, Technical University of Denmark, 2800 Kgs. Lyngby, Denmark*
²*Departamento de Física, Universidade Federal de Minas Gerais, C. P. 702, 30123-970, Belo Horizonte, MG, Brazil*
³*Swiss Light Source, Paul Scherrer Institut, CH-5232 Villigen, Switzerland*
⁴*Department of Physics, Technical University of Denmark, 2800 Kgs. Lyngby, Denmark*

Strontium niobate has triggered a lot of interest as a transparent conductor and as a possible realization of a correlated Dirac semimetal. Using the lattice parameters as a tunable knob, the energy landscape of octahedral tilting was mapped using density functional theory calculations. We find that biaxial compressive strain induces tilting around the out-of-plane axis, while tensile strain induces tilting around the two in-plane axes. The two competing distorted structures for compressive strain show semi-Dirac dispersions above the Fermi level in their electronic structure. Our density functional theory calculations combined with dynamical mean field theory reveal that dynamical correlations downshift these semi-Dirac-like cones towards the Fermi energy. More generally, our study reveals that the competition between the *in-phase* and *out-of-phase* tilting in SrNbO₃ provides a new degree of freedom that allows for tuning the thermoelectric and optical properties. We show how the tilt angle and mode are reflected in the behavior of the Seebeck coefficient and the plasma frequency due to changes in the band structure.

I. INTRODUCTION

The perovskite (oxide) structure, ABO_3, is a versatile structure relevant in many existing and emerging applications [1] including piezoelectricity [2], thermoelectricity [3], oxygen separation, and solid oxide fuel cells [4]. It is also a platform where the coupling of charge, spin, and orbital degrees of freedom takes place, giving rise to numerous materials with interesting electronic and magnetic properties such as superconductivity [5], colossal magnetoresistance [6], metal-insulator transitions [7,8], and more recently the realization of correlated Dirac semimetallic states [9].

One possible way of changing the properties of perovskite oxides is to apply strain to the crystal [10,11]. This can be achieved by epitaxial growth of films on substrates with different lattice parameters. The lattice mismatch between the substrate and the film will induce strain in the system. The compression (tension) induced by the substrate will shrink (expand) the in-plane B-O bond length from its equilibrium value. As a response, the oxygen ions can displace and alter the B-O-B bond angle and bond lengths, and in this way relieve stress. This displacement will be referred to as *octahedral tilt* or *octahedral rotation*, and it is visualized in Fig. 1.

Strontium niobate, SrNbO₃, is a conducting perovskite oxide that has gained interest in recent years [9,12–14]. SrNbO₃ has a larger lattice parameter in comparison to the prototypical SrTiO₃, i.e., 4.023 and 3.905 Å, respectively [12]. Park *et al.* investigated SrNbO₃ as a potential transparent conductor due to its large gap between the (filled) conduction and valence states [14]. The energy gap between the valence-band maximum and the conduction-band minimum is ∼2.3 eV, predicted with density functional theory in Ref. [14]. Further interest has been related to the emerging Dirac states in heavily strained SrNbO₃ thin films. Both theoretical and experimental work suggests that light electrons emerge in strained SrNbO₃ films due to the induced octahedral tilting [9].

Yet, there has been no systematic investigation of the atomic and electronic structure of SrNbO₃ under biaxial stress, e.g., found in epitaxial thin films, especially including octahedral tilting. Theoretical calculations provide a fast and unique way to investigate the local distortions, which are difficult to access using experimental techniques [15]. This has been shown to be important for explaining metal-insulator behavior in 3d perovskite oxides using standard density functional theory (DFT) methods [16]. Distortions such as octahedral tilting alter the electronic configuration, specifically the orbital overlaps and bandwidths, W. The ratio between the interelectronic Coulomb interaction and the bandwidth, U/W, describes the strength of the electron correlation. Furthermore, a large ratio can result in a localization of the electrons, i.e., U/W governs the Mott metal-insulator transition [17]. Hence, the electrical properties are dependent on the bandwidth, which is connected to distortions such as octahedral tilting. Similarly, there is a connection between the bandwidth and the optical response of a material. The plasma
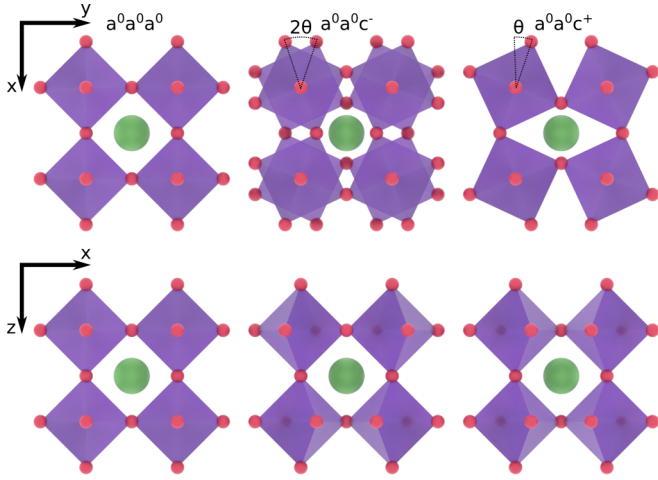
---

*vicros@dtu.dk
†nipr@dtu.dk

FIG. 1. Illustration of different octahedral tilting modes. The left column shows $a^0a^0a^0$ (no tilt), the middle column shows $a^0a^0c^-$ (*out-of-phase* tilting), and the right column shows $a^0a^0c^+$ (*in-phase* tilting). The upper (lower) row shows the structures in the xy-plane (zx-plane). In the SrNbO$_3$ structure, the octahedra are formed by oxygen (red) centered around niobium atoms. The green spheres correspond to strontium atoms.

frequency that governs the optical response can be written as $\omega_p = e\sqrt{n/(m^*\varepsilon)}$, with e being the elemental charge, n is the carrier concentration, m^* is the effective mass, and ε is the permittivity [13,18]. The plasma frequency is then related to the bandwidth through the effective mass $m^* \propto 1/W$. Therefore, a reduction of the bandwidth (or increase in effective mass) results in a redshift of the plasma frequency. Due to the connection between atomic structure and electrical and optical properties discussed here, it is worthwhile to consider the influence of octahedral tilting on the material properties of SrNbO$_3$.

In this study, we first address the atomic and electronic structure for SrNbO$_3$ as a function of epitaxial strain using DFT. Since SrTiO$_3$ is a very common substrate for growing perovskite oxides and has been investigated extensively before, we used it as a reference for all calculations. Both compressive and tensile biaxial strain is considered, and the applied strain is always in the (001)-plane of SrTiO$_3$ and SrNbO$_3$. Different octahedral tilts have been investigated with respect to the imposed strain, and the stabilization of the different octahedral tilts with respect to doping was analyzed. Furthermore, we investigate how the excitation spectra and degree of electronic correlations of SrNbO$_3$ evolve as a function of octahedral tilting. The Seebeck coefficient and the optical loss function have been studied for relevant octahedral tilting modes and angles. We aimed at establishing a complete picture of octahedral tilting in SrNbO$_3$ for various strains.

II. COMPUTATIONAL METHODS

Density functional theory (DFT) [19] was used to investigate the atomic and electronic structures of SrNbO$_3$ (and SrTiO$_3$). Our DFT calculations were performed using the exchange-correlation functional PBEsol, and projector augmented wave (PAW) potentials [20,21] as implemented in *Vienna Ab initio Simulation Package* (VASP) [22]. The

PBEsol functional was chosen due to its ability to predict accurate lattice parameters as pointed out in Refs. [23,24]. The total energies were calculated with Γ-centered k-point meshes $8 \times 8 \times 8$ and $4 \times 4 \times 4$ for the primitive (5-atom) cell and $2 \times 2 \times 2$ (40-atom) supercell, respectively. The self-consistent loops were converged below 1×10^{-6} eV and the plane-wave energy cutoff was set to 550 eV. A force tolerance of 0.01 eV/Å was set during the relaxations. Octahedral tilts were introduced to the $2 \times 2 \times 2$ supercells by moving the oxygen ions according to $\delta = \tan(\theta)(a/2)$, where δ is the displacement due to a rotation and $a/2$ is the B-O distance, expressed by the lattice parameter, a. A rotation around, e.g., the z-axis would result in a shift $\pm\delta$ in x for the oxygen ions on the y-axis, and vice versa. The sign alternates between each adjacent octahedra in the xy-plane (and also between each layer in the z-direction for out-of-phase tilting). The space groups of the tilted structures were checked using spglib [25].

Using the DFT obtained relaxed structures, we performed DFT plus dynamical mean field theory (DMFT) calculations at 200 K for SrNbO$_3$ using the *state-of-the-art* fully charge self-consistent implementation [26]. The DFT part was done within the Perdew-Burke-Ernzerhof generalized gradient approximation (PBE-GGA) [27] as implemented in the WIEN2K package [28]. Within our implementation, we take into account all the itinerant and correlated states (Nb-t_{2g}) within a large energy window (20 eV) around the chemical potential. This is done using a projector that preserves both causality and spectral weight as proposed in Ref. [26]. The DMFT impurity problem was solved by using continuous-time quantum Monte Carlo (CTQMC) calculations [29], with a Hubbard $U = 6.0$ eV and Hund's coupling $J = 0.8$ eV. These values are chosen since they are similar to the ones used in previously published DFT+DMFT studies of SrNbO$_3$ [13,14]. To compute the spectral functions, we performed the analytical continuation of the self-energy using the maximum entropy method [26].

The Seebeck coefficient was predicted within the constant relaxation-time approximation employing BOLTZTRAP2 [30]. This was done using a charge density calculated with a k-point density corresponding to $15 \times 15 \times 15$ for the 5-atom cubic unit cell. Non-self-consistent calculations were performed using a k-point mesh of $50 \times 50 \times 50$ for the 5-atom cubic unit cell. The electronic states were then interpolated on a grid 15 times as dense using BOLTZTRAP2. The temperature was set to 300 K.

The complex dielectric function was calculated using the independent-particle random phase approximation (RPA) as implemented in VASP. This implies that the excitations are assumed to be independent, given by the bare Kohn-Sham band structure and neglect of the local field effects [31]. A phenomenological Drude term was added to model the contribution of intraband transitions; see Appendix B. The imaginary part was set to 0.3 eV, which creates good agreement with experimental loss functions in Ref. [18].

III. RESULTS AND DISCUSSIONS

A. Energy landscape of octahedral tilts

The lattice parameters for varying degrees of biaxial strain were calculated for SrNbO$_3$. This was done
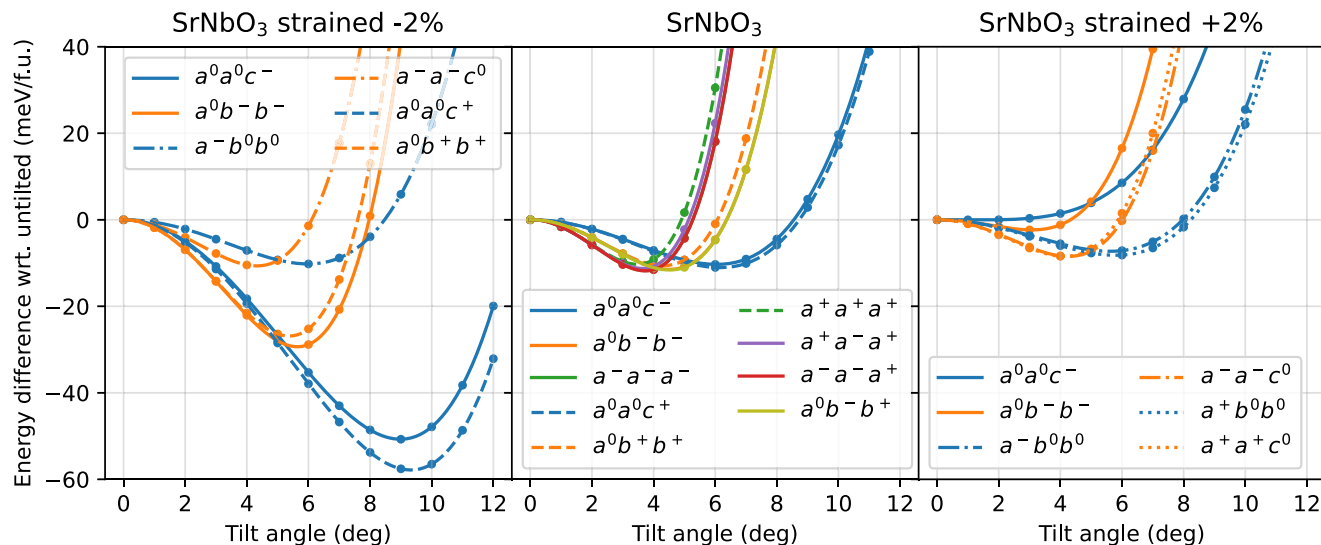
FIG. 2. Energy landscapes of octahedral tilting in SrNbO$_3$ under different amounts of biaxial strain. The energy shown is the difference in total internal energy between the tilted structure and untilted structure. The middle plot is the case of no biaxial strain. Compressive strain stabilizes the tilts around the out-of-plane axis, while tensile strain leads to preferred rotations around the in-plane axes. The *in-phase* tilt $a^0a^0c^+$ is found to have the largest energy gain in compressively strained SrNbO$_3$.

using the high-symmetry 5-atom unit cells, i.e., excluding any symmetry-breaking octahedral tilting. The relative difference, $(a_{\mathrm{DFT}} - a_{\mathrm{exp}})/a_{\mathrm{exp}}$, was $\sim -0.15\%$ for unstrained SrNbO$_3$. Here, $a_{\mathrm{DFT}} = 4.0182\,\text{Å}$ and $a_{\mathrm{exp}} = 4.023\,\text{Å}$ [12] are the predicted and experimental unstrained lattice parameters, respectively. A table of the relaxed out-of-plane lattice parameters for different biaxial strains between -3% and $+3\%$ can be found in Appendix A. These lattice parameters were fixed throughout the rest of the study.

Using the calculated lattice parameters, we predicted the energy landscapes of the octahedral tilting for varying degrees of strain. In the case of unstrained SrNbO$_3$ (and SrTiO$_3$) the following pure octahedral tilts were investigated (using Glazer's notation [32]): $a^0a^0c^-$, $a^0a^0c^+$, $a^0b^-b^-$, $a^0b^+b^+$, $a^-a^-a^-$, and $a^+a^+a^+$. Combined *in-phase* and *out-of-phase* tilts were also sampled, e.g., $a^+a^-a^+$, $a^-a^-a^+$, and $a^0b^-b^+$. The letters a, b, and c correspond to the rotation angles around the x, y, and z axis, respectively, and the $+/-$ signs denote *in-phase* and *out-of-phase* rotation between two adjacent octahedra; see Fig. 1. The superscript 0 denotes that no rotation is performed around that Cartesian axis. For the strained systems, we examined octahedral tilts around both the *in-plane* and *out-of-plane* axes, since they are no longer symmetrically equivalent. These calculations were performed on fixed tilts, i.e., for each structure the energy was only evaluated once (self-consistently) without any update of the atomic positions. In this work, we generally did not consider tilts with different angles around different axes, i.e., it is assumed that the rotation angles are the same around all axes (except if one or more is zero). However, since neutron diffraction studies of SrNbO$_3$ have shown indications of the $a^-a^-c^+$ tilt mode [33], this mode was investigated additionally. To check if $a^-a^-c^+$ is preferred over $a^-a^-a^+$, we varied the rotation angles θ_a and θ_c for $a^-a^-c^+$. The energy was never below the $a^-a^-a^+$ mode with tilt angle $4°$, i.e., $a^-a^-c^+$ is not preferred over

$a^-a^-a^+$. However, since the energy landscape of unstrained SrNbO$_3$ is rather shallow, it is possible that SrNbO$_3$ might condense into any of the competing modes, including more general modes such as $a^-a^-c^+$ with different rotation angles around the different axes. Furthermore, the stability of $a^0a^0c^+$ and $a^0a^0c^-$ was confirmed in the case of compressive strain by including a small rotation around the x and the y axis. Minimizing the ionic forces led to a suppression of these rotations, which suggests that the lowest energies are in fact found for systems with rotation *only* around the *out-of-plane* axis in the case of compressive strain.

Figure 2 shows the total internal energy landscapes for different octahedral tilts in SrNbO$_3$ under varying degrees of strain. The reference energy is the total internal energy of the untilted structures, so that the energy goes to zero at zero tilt angle (each strain has its own reference energy). For unstrained SrNbO$_3$, all octahedral tilts show an energy reduction, including the *in-phase* tilting modes. This is not the case for the unstrained SrTiO$_3$ (see Fig. 3 or Appendix F). This is a notable feature, since the *in-phase* tilting is rare in oxide perovskites [34]. Furthermore, the energy gain is larger than in SrTiO$_3$ and the optimal tilt angles are also slightly larger. For -2% strained SrNbO$_3$ (SrTiO$_3$) the $a^0a^0c^-$ tilt mode shows a gain of $\sim 50\,\text{meV f.u.}^{-1}$ ($30\,\text{meV f.u.}^{-1}$) compared to the untilted phase, and the optimal tilt angle is $\sim 9°$ ($7.5°$). The complete data set for SrTiO$_3$ and SrNbO$_3$ with additional strain values can be found in Appendix F.

By biaxially compressing the oxides (while relaxing the out-of-plane lattice parameter) the B-O bond length in the octahedral structure is contracted in-plane and extended out-of-plane. As a result, the oxygen network is distorted by octahedral tilting. This phenomenon can be seen in the left plot in Fig. 2, where the crystals are biaxially strained by -2% (with the out-of-plane lattice parameters relaxed; further details are given in Table I in Appendix A). The key messages
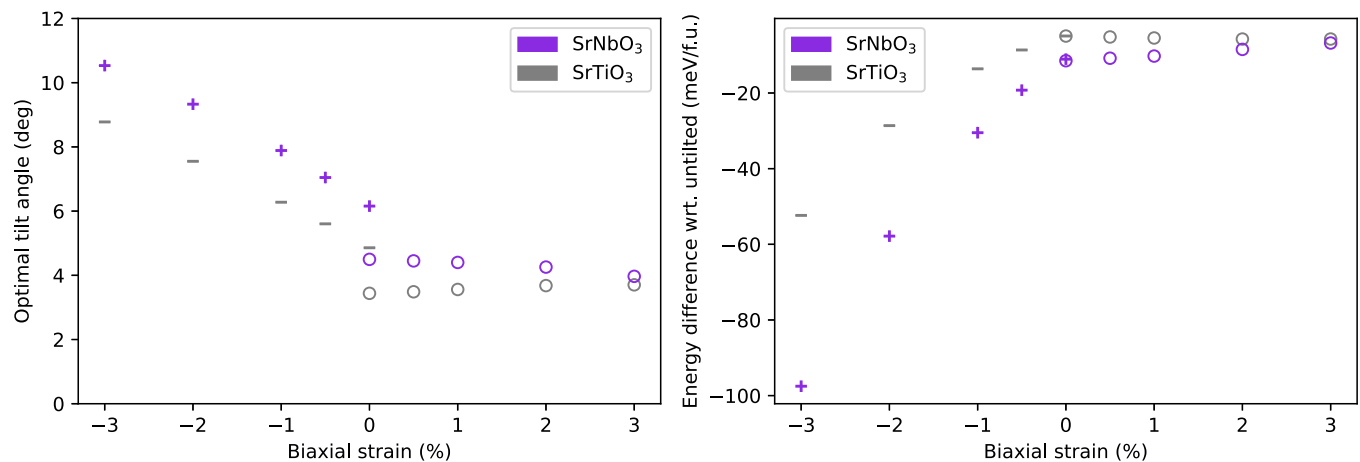
FIG. 3. Optimal tilt angles for SrNbO$_3$ and SrTiO$_3$ with varying biaxial strain. A plus (minus) sign means that the $a^0a^0c^+$ ($a^0a^0c^-$) tilt mode is lowest in energy, i.e., for SrNbO$_3$ the $a^0a^0c^+$ mode is lowest in energy under compressive strain. The circle marker denotes the $a^-a^-c^0$ tilting mode, which is the stable tilt under tensile strain. For 0% we include multiple data points, since the energies are very similar and it helps with understanding the limit from compressive to unstrained and tensile to unstrained.

are (i) due to the tetragonality, octahedral tilting is preferred around the (longer) out-of-plane axis, (ii) tilts around one and two axes are no longer degenerate (likely due to competition between B-O and A-O bond lengths, e.g., the A-O bond length is shorter for $a^0b^-b^-$ than $a^0a^0c^-$ and the B-O bond lengths are only slightly longer for $a^0b^-b^-$ than $a^0a^0c^-$), and (iii) *in-phase* tilts are energetically favorable for strained SrNbO$_3$, in contrast to SrTiO$_3$ where *out-of-phase* tilting is favorable. The energy gain for *in-phase* tilting relative to *out-of-phase* tilting in SrNbO$_3$ increases with larger biaxial compressive strain; see Appendix F. This behavior is interesting, because perovskite oxides typically show preference for *out-of-phase* tilting [34]. Furthermore, in a recent study where SrNbO$_3$ thin film was grown on SrTiO$_3$, x-ray diffraction experiments suggested that the $a^0a^0c^-$ tilting mode is stabilized under compressive strain [9].

Biaxial tensile stress elongates the lattice in-plane while the lattice contracts out-of-plane; see Table I. The resulting energy landscapes with respect to octahedral tilting for +2% biaxially strained SrNbO$_3$ is shown in Fig. 2. The calculated wells are quite shallow compared to the case of compressive strain; instead their depths are similar to the unstrained case. During tensile strain, the two in-plane lattice parameters are found to increase and the out-of-plane lattice parameter decreases. Therefore, oxygen octahedral tilting can only alleviate stress in one direction (out-of-plane) by octahedral rotation around the two in-plane axes. In other words, tensile biaxial strain leads to octahedral tilting around the in-plane axes, in contrast with compressive biaxial strain, which leads to tilting around the out-of-plane axis, in agreement with investigations of other perovskite oxides [35,36]. Due to the small energy gains observed here for tensile strained SrNbO$_3$, the possibility of stabilizing octahedral tilting by tensile strain is quite small, especially at elevated temperatures.

The overall optimal tilt modes and their magnitudes are shown in Fig. 3. Here we include SrTiO$_3$ as a reference. It is seen that the octahedral tilting is energetically more stable in the case of SrNbO$_3$ than for the case of SrTiO$_3$ (see also

Appendix F). The optimal tilt angles are ∼25% larger in SrNbO$_3$ than SrTiO$_3$, which is true under compressive strain and small tensile strains. For larger tensile strains, the two materials show similar tilting behavior. It is interesting to note that the trends are reversed in tensile strained SrNbO$_3$ and SrTiO$_3$. Larger tensile strain is found to destabilize the tilting (both smaller energy gains and rotation angles) in SrNbO$_3$. The opposite is found in SrTiO$_3$.

In perovskite oxides, *out-of-phase* tilting (or tilts with both *in-phase* and *out-of-phase* components) is the most prevalent tilting mode. Young and Rondinelli [34] studied bromide and iodide perovskites and linked the octahedral tilt stability to electrostatic interactions, bond valency sums of the A-site ions, and charge distribution between the A-site ions and the cations. Here, the A-site ions are not displaced during octahedral tilting, hence the bond valency remains constant when comparing *out-of-phase* ($a^0a^0c^-$) and *in-phase* ($a^0a^0c^+$) tilts. This is because the bond valency is a function of the nearest-neighbor distances only.

To understand what stabilizes the *in-phase* tilt in SrNbO$_3$ and SrTiO$_3$, we controlled the doping by creating holes in SrNbO$_3$ and adding electrons in the case of SrTiO$_3$. We added (or removed) charge in steps of 0.25 electrons per formula unit up to 1 electron per formula unit. This was achieved using the background charge method, which allows for modeling of doping without having to introduce impurities by the use of supercells. Charge neutrality is kept by the introduction of a homogeneous background charge. While this method has its flaws, such as inaccurate lattice relaxations [37], it allows us to get some insight into the stability of tilting without more elaborate calculations. The lattice is kept fixed while analyzing the influence of doping, and only the oxygen ions are displaced. Additional electrons can increase the energy gain by octahedral tilting in SrTiO$_3$, as indicated in Ref. [38]. Hence, octahedral tilting is stabilized with the addition of electrons in SrTiO$_3$. Uchida *et al.* [38] attribute the stabilization of the tilting to the increase in size of the Ti ion, hence decreasing the Goldschmidt factor. The Goldschmidt tolerance factor,
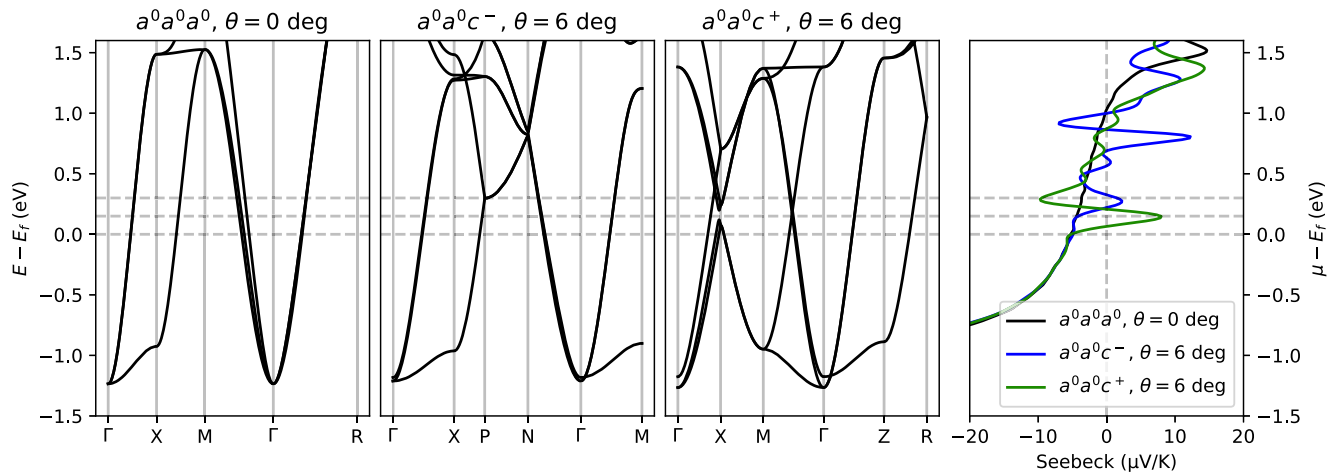
FIG. 4. Conduction bands of unstrained SrNbO$_3$ with $a^0a^0a^0$, $a^0a^0c^-$, and $a^0a^0c^+$ tilt modes. The tilt angle, θ, is set to 6°. To the right, the in-plane Seebeck coefficient as a function of chemical potential at 300 K is shown. The peaks in the Seebeck coefficient align with the (avoided) band crossings at P for $a^0a^0c^-$ and at X as well as along M-Γ for $a^0a^0c^+$. The Γ-point t_{2g} split is sensitive to the tilting mode. For $a^0a^0a^0$, the t_{2g} states are degenerate at Γ. The degeneracy is lifted for $a^0a^0c^-$ and $a^0a^0c^+$. The Brillouin zones, with sampled high-symmetry points, for the different tilting modes can be found in Appendix C.

$t = (r_A + r_O)/[\sqrt{2}(r_B + r_O)]$, where r_i denotes the ionic radius of ion i, indicates the stability of octahedral distortions in perovskite oxides [39]. In the following, we will focus only on -2% strained system since it is a relevant strain observed in thin films. The resulting energy landscapes are shown in Fig. 10 in Appendix D. By analyzing both the $a^0a^0c^-$ and the $a^0a^0c^+$ tilting modes, it is evident that including electrons reduces the energy difference between the two tilt modes. To the best of our knowledge, this has not been considered in earlier works. On the contrary, introducing holes to SrNbO$_3$ is found to destabilize the two tilt modes. Here, as in the case of SrTiO$_3$, changing the number of electrons (by addition of holes) also changes the energy difference between the two tilt modes. Interestingly, there is a critical point at which $a^0a^0c^-$ is stabilized over $a^0a^0c^+$ in SrNbO$_3$ (see Fig. 10). Adding 0.5 holes per formula unit, i.e., 0.5 holes per Nb ion, to SrNbO$_3$ makes the two tilt modes almost degenerate with a slight preference for $a^0a^0c^-$ over $a^0a^0c^+$.

This suggests that the stability of the *out-of-phase* ($a^0a^0c^-$) and *in-phase* ($a^0a^0c^+$) tilting modes is connected to the number of electrons and the size of the A ion (e.g., Nb and Ti). Further investigations by doping with different ion sizes could benefit our understanding of the stability of the various tilting modes in more complex scenarios. These results also suggest that the so-called rigid-band assumption should be used with caution for perovskites. In other words, it is possible that electron doping affects the octahedral tilting stability, hence the assumption that doping can be captured by a simple shift of Fermi level is questionable. In summary, these predictions suggest that it is possible to tune the stability of octahedral tilting by doping and/or gating.

The effect of dynamical correlations on the octahedral tilting was briefly investigated by calculating the total energy landscape of -2% strained SrNbO$_3$ using DFT+DMFT. We note that the free energy and total energy landscapes are very similar, and therefore we focus only on the latter. Here, we

limited ourselves to $a^0a^0c^-$ and $a^0a^0c^+$. The total energy landscapes are qualitatively similar to the ones predicted using DFT, i.e., both tilt modes show stabilization and $a^0a^0c^+$ is preferred over $a^0a^0c^-$. However, the energy gains and optimal tilt angles are larger for DFT+DMFT compared to DFT. The $a^0a^0c^+$ mode shows an energy gain of ~ 100 meV f.u.$^{-1}$ with a tilt angle of $\sim 10°$ within the DFT+DMFT framework. This is a substantial increase compared to DFT, and it is something to consider in future work related to octahedral tilting in oxides. However, since the qualitative trends are similar, we do not consider this further in this work.

B. Effects of tilt and strain on band structure and spectral function

We then moved over to the electronic structure of SrNbO$_3$. The electronic band structure of SrNbO$_3$ was studied with different octahedral tiltings. Here, we focus on $a^0a^0c^-$ and $a^0a^0c^+$ since they are both stabilized under compressive biaxial strain. The reference in these cases was the untilted ($a^0a^0a^0$) SrNbO$_3$.

In Fig. 4 the conduction bands for unstrained SrNbO$_3$ are shown for different octahedral tilts. The band structures are calculated along high-symmetry points of the first Brillouin zone for the different crystals (see Appendix C for Brillouin zones). Here, the rotation angle is set to 6°, which is close to the minima for $a^0a^0c^-$ and $a^0a^0c^+$ in the unstrained case. The untilted system shows the heavy and light bands which originate from the t_{2g}-like niobium orbitals. Since the tilts require repetitions of the minimal unit cell, there are additional bands in $a^0a^0c^-$ and $a^0a^0c^+$. The *out-of-phase* tilt $a^0a^0c^-$ shows a semi-Dirac point at P, in agreement with Ref. [9]. This tilt mode has been further investigated theoretically illustrating the tunability of the Berry phase and the anomalous Hall coefficient [40]. A similar dispersion is found at the X-point in $a^0a^0c^+$, albeit at a substantially higher energy. Both tilt modes
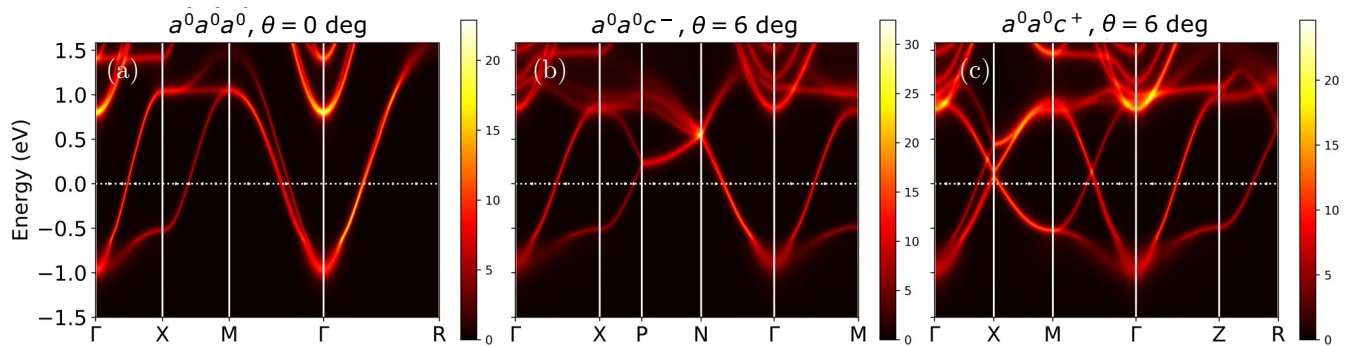
FIG. 5. DFT+DMFT calculated spectral functions at 200 K of unstrained $SrNbO_3$ with $a^0a^0a^0$ (a), $a^0a^0c^-$ (b), and $a^0a^0c^+$ (c) tilt modes.

create t_{2g} splitting at the Γ-point, however for $a^0a^0c^-$ with 6° rotation angle the splitting is quite small. The *in-phase* tilt $a^0a^0c^+$ shows a gap opening at the X-point slightly above the Fermi level. The band velocities are low at the bottom of the conduction bands and higher near the Fermi level, as can be seen from the slope of the bands ($\hbar v_{\mathbf{k}} = \partial_{\mathbf{k}}\epsilon_{\mathbf{k}}$). Moreover, the bands near the Dirac points show both mobile and slow carriers, as indicated by the slopes of the bands. As an example, the states from P to X show high velocities, while the opposite is true for the states from P towards N in the case of $a^0a^0c^-$.

The qualitative picture of the band structure is rather similar for compressively strained $SrNbO_3$ (see Appendix G). There are, however, a few noteworthy changes. Straining introduces t_{2g} splitting in the untilted system, due to a symmetry lowering from cubic to tetragonal. Inclusion of octahedral tilting further splits the t_{2g} states. For -2% strained $SrNbO_3$, the split is ~ 0.15 and 0.3 eV for $a^0a^0c^-$ and $a^0a^0c^+$, respectively, both with a 9° tilt angle. By examining the splitting for different strain-tilt combinations, it is observed that the large t_{2g} splitting in strained $SrNbO_3$ originates from both the strain alone and from the increase in tilt angle with strain. The t_{2g} splitting at the Γ point can be found in Appendix E. As an example, the t_{2g} splitting in -1% strained $a^0a^0a^0$ is ~ 0.05 eV and is of similar magnitude to the splitting in unstrained $a^0a^0c^+$ with a 6° tilt angle. Furthermore, the Dirac point at P is shifted closer to the Fermi level for $a^0a^0c^-$ with compressive strain, while the gapping at X is larger in the case of -2% strained $a^0a^0c^+$ with a 9° rotation angle than unstrained $a^0a^0c^+$ with 6°. The increase in the gap at X is dominated by the enhancement of the tilt angle with strain, i.e., the gap is not so sensitive to the strain alone. We speculate that it in fact may be the t_{2g} splitting that stabilizes the $a^0a^0c^+$ tilt mode by decreasing the lowest conduction-band energies at the Γ-point and creating a gap at X, compared to the other modes; see Fig. 4.

In Fig. 5, we present the DFT+DMFT obtained spectral functions. As can be noticed, the dynamical correlations downshift the Dirac-like points toward the Fermi level. The P and N crossing points exhibited in the $a^0a^0c^-$ structure are ~ 0.25 and 0.55 eV above the Fermi energy, compared to 0.30 and 0.75 eV, respectively, in the DFT band structure. Furthermore, we observe an additional crossing point at 0.27 eV along Γ-X in $a^0a^0c^+$ structure. The Dirac point between M-Γ appears around 0.15 eV.

Overall, these findings indicate that the interplay of lattice distortions and electronic correlations is a key factor for the topology properties of strained $SrNbO_3$ thin films. This analysis also illustrates the tunability of the electronic states in $SrNbO_3$ with biaxial compressive strain. The tunability has two components: there is an effect from straining alone, but also an effect from the tilt that is induced by the strain. Furthermore, since the stability of the octahedral tilting modes seems to be connected to the number of electrons, it could also act as a turning knob for the atomic structure and hence electronic structure in addition to a shift of Fermi level.

C. Seebeck coefficient and optical properties

We further investigated the influence of the octahedral tilting on the Seebeck coefficient. The Seebeck coefficient was selected as a useful probe of the electronic structure of the material. In comparison to the conductivity or mobility, the Seebeck coefficient is less sensitive to the scattering rate. Specifically, in the constant relaxation-time approximation, the Seebeck coefficient is independent of the scattering rate [30]. Therefore, changes in the band structure could have an effect on the Seebeck coefficient, which could act as a fingerprint for the octahedral tilting. In Fig. 6, the in-plane (i.e., $xx = yy$ component) Seebeck coefficient is shown for the two tilts as a function of octahedral rotation angle. The results are shown for unstrained $SrNbO_3$ at a temperature of 300 K. The qualitative trends are the same for -2% strained $SrNbO_3$. Below ~ -100 meV all configurations show a negative Seebeck coefficient lower than $-5\,\mu V\,K^{-1}$, corresponding to n-type transport. The typical Seebeck coefficients for metals or heavily doped semiconductors are $\pm 10\,\mu V\,K^{-1}$ [41]. Interestingly, near the Fermi level and slightly above, the Seebeck coefficient varies and can even become positive when octahedral tilting is included. Furthermore, this behavior is different for $a^0a^0c^-$ and $a^0a^0c^+$. The positive values occur at lower energies for $a^0a^0c^+$ than $a^0a^0c^-$. In the case of $a^0a^0c^+$ there is also a sharp decrease in the Seebeck coefficient after the increase with higher chemical potential. These features can be connected to the band crossings in Fig. 4. The semi-Dirac point at P coincides with the first Seebeck peak in the case of $a^0a^0c^-$. Similarly, in the case of $a^0a^0c^+$ the first peak coincides with the gapped bands at X and the cluster of bands along M-Γ. The sign of the Seebeck coefficient is sensitive to
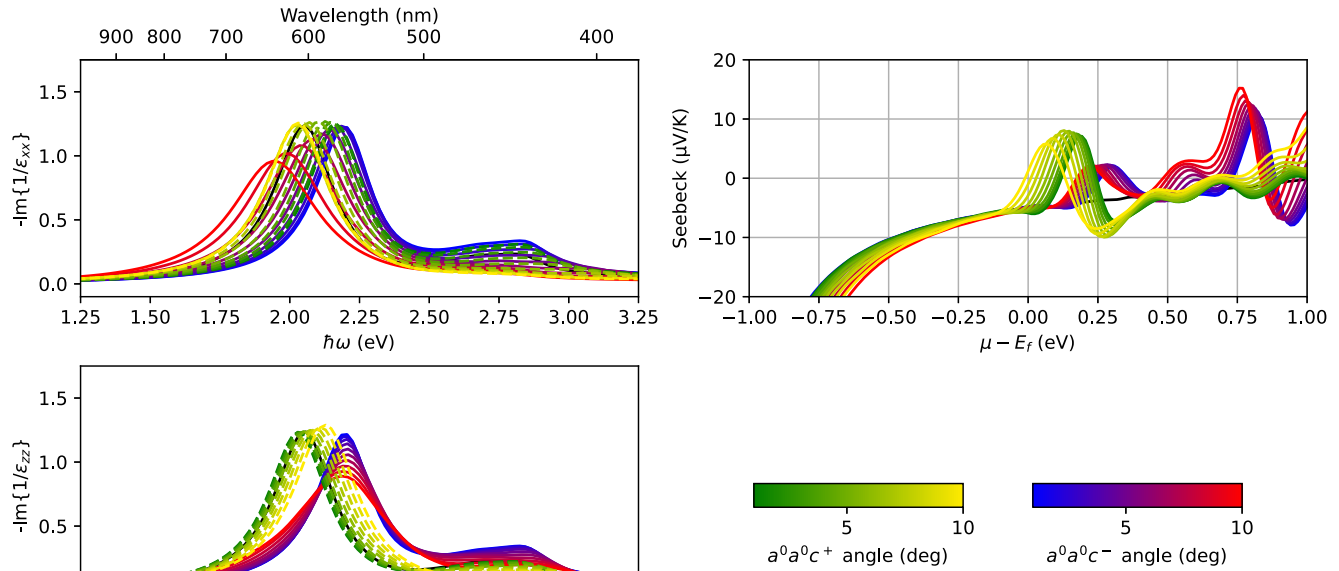
FIG. 6. Influence of octahedral tilting on the optical loss function (top left and bottom left) and on the room-temperature in-plane Seebeck coefficient (top right) in unstrained SrNbO₃. The black lines correspond to the response of untilted SrNbO₃. In the upper left (lower left) figure, the xx (zz) component of the optical loss function is shown. For visibility, the $a^0a^0c^+$ tilts are drawn with a dashed line. A systematic redshift with a tilt angle is observed in the loss peak of the xx component, while the zz component shows a blueshift with a tilt angle of $a^0a^0c^+$ and an almost constant peak position for $a^0a^0c^-$. Due to the (avoided) band crossings related to octahedral tilting, the Seebeck coefficient shows sign changes over a small range of chemical potentials.

the character of the dispersion, such as nonparabolic features and band crossings, as indicated in Ref. [42] for graphene. This highlights the difference between the effects of strain and octahedral tilting, since strain alone does not create new features such as band crossings and gapping near the Fermi level. The Seebeck values are, of course, small, i.e., not relevant for thermoelectric generator purposes, but they could be valuable as fingerprints of octahedral tilting. Measurements of the Seebeck coefficient, with varying gate voltage, of SrNbO₃ could be used as an indirect probe of the electronic structure. Abrupt sign changes, with respect to chemical potential, could be used as a fingerprint of octahedral tilting and an indication of change in the topology of the bands, compared to the bands of untilted SrNbO₃ that show a much flatter change in Seebeck with respect to chemical potential.

We then examined the optical properties of SrNbO₃ for different octahedral tilting by calculating the optical loss function. The optical loss function, which describes the interaction between electromagnetic fields and matter, is an indirect probe of the electronic states. The optical loss function can be written as $LF(\omega) = -Im\{\epsilon(q \to 0, \omega)^{-1}\}$, where the optical limit $q \to 0$ of the dielectric function, $\epsilon(\omega)$, results in no momentum transfer between the applied field and the electrons. The loss function exhibits a peak when the real part of the dielectric function changes sign (a slight energy shift can occur due to the frequency-dependent imaginary part). Therefore, the loss function peak position is a good indication of the plasma frequency defined by $Re\{\epsilon(\omega_p)\} = 0$. The optical loss functions given by the independent-particle random phase

approximation are shown in Fig. 6 for unstrained SrNbO₃. Both xx and zz components of the loss functions are shown. A clear loss peak is observed in the visible regime for each tilt configuration, in agreement with Refs. [14,18]. Therefore, the plasma frequencies are in the visible regime. Increasing the rotation angle in $a^0a^0c^-$ decreases the peak height for the xx and zz components. Furthermore, there is a redshift of the peak (and hence plasma frequency) of the xx component, while this is not true for the zz component. Contrary to this, the peak height seems not to be sensitive to variations of the $a^0a^0c^+$ rotation angle. There is also a redshift of the peak and plasma frequency for $a^0a^0c^+$ with larger rotation angles when the xx component is considered. The opposite is true in the zz component, i.e., there is a blueshift of the plasma frequency with respect to larger rotation angles for $a^0a^0c^+$. For smaller octahedral rotations, there is also a secondary peak at ∼2.75 eV. This peak has been connected to the excitations from t_{2g} to e_g bands [13,14], and it is weakened with a larger rotation angle, especially for the xx component. The peaks vanish for large rotations for both $a^0a^0c^-$ and $a^0a^0c^+$. It has been noted that the small peak is absent in experiments, while it is present in DFT. This fits well with our predictions, since octahedral tilting breaks the octahedral crystal field, i.e., the t_{2g} and e_g states are altered by octahedral tilting. One should, however, further analyze the transmission matrix elements between these states, with various tilting, for a complete picture. To our knowledge, octahedral tilting was not included in the DFT analysis by Park and co-workers [14]. It is possible that the missing secondary peak in spectroscopic ellipsometry

at room temperature is due to thermally fluctuating oxygen ions in the $SrNbO_3$ rather than stabilization of a tilting mode. Furthermore, it is possible that correlation effects, such as finite lifetimes and renormalization, could influence the details of the optical response, including the peak at $\sim$2.75 eV. In any case, temperature-dependent spectroscopic ellipsometry could be valuable for understanding the stabilization of the octahedral tilting modes, given the strong signals due to tilting predicted here and the energy scale involved, which is comparable to the thermal energy.

The effect of biaxial strain on the optical properties of $SrNbO_3$ (and other oxides) was investigated previously by Paul and Birol [13]. They showed that the plasma frequency is almost constant in zz, while there is a systematic blueshift of the xx component with compressive strain. Furthermore, Paul and Birol showed how renormalization of the effective mass due to correlations can redshift the plasma frequency according to the expression $\omega_p = e\sqrt{n/(m^*\varepsilon)}$. Our predictions show that octahedral tilting could shift the plasma frequency substantially (between 2.0 and 2.25 eV), which could be interpreted as a mass renormalization, not due to dynamic correlations but due to octahedral tilting. Here, the sign (i.e., redshift or blueshift) is sensitive to what octahedral tilting mode is present and which component of the dielectric function one is sensing, i.e., xx or zz. This further illustrates the need for systematic temperature-dependent spectroscopic ellipsometry of $SrNbO_3$ under varying strain.

The independent particle assumption used in the calculation of the dielectric function is relatively crude, but it has been shown to qualitatively reproduce the experimental plasmon peak in $SrNbO_3$ when intraband transitions are included [43]. We modeled intraband transitions by using a phenomenological Drude term (see Appendix B). Although these calculations involve serious approximations, they indicate how some typical experimental quantities can give a fingerprint of the underlying octahedral tilting.

These observations call for further *ab initio* modeling of $SrNbO_3$ (and other perovskites), not only by assuming highly symmetric unit cells, but also allowing for deviations from highly symmetric cells by the use of supercells [15]. Further investigations of the stabilization of octahedral tilting with respect to strain under finite temperatures will be highly relevant for application purposes. Our results show that octahedral tilting can have a significant effect on thermoelectric and optical properties. The Seebeck coefficient exhibits sign changes due to the new band features appearing from the octahedral tilting. Moreover, the optical loss function peak position and plasma frequency are tuneable by octahedral tilting over a range of $\sim$100 nm in the visible regime. Therefore, octahedral tilting should be considered when analyzing strained perovskite oxides like $SrNbO_3$.

IV. CONCLUSIONS

A first-principles investigation of the atomic and electronic structure of $SrNbO_3$ under biaxial strain has been performed with emphasis on the relation between octahedral tilting and strain. This was done by using supercells to allow for the symmetry-breaking octahedral tilting, while the biaxial strain was applied in the (001) plane. By methodically sampling different tilt modes and magnitudes, the optimal octahedral tilting could be found for the different strain conditions. Compressive (tensile) strain was found to induce octahedral tilting around the out-of-plane (in-plane) axis. Interestingly, the *in-phase* tilt $a^0a^0c^+$ was energetically favorable for $SrNbO_3$ under compressive strain. This is in contrast to $a^0a^0c^-$, which has been reported in a recent experimental study of $SrNbO_3$ [9]. The *in-phase* tilt, $a^0a^0c^+$, shows larger t_{2g} splitting compared to the *out-of-phase* tilt $a^0a^0c^-$. The electronic dispersion is also gapped slightly above the Fermi level at the X-point, in the case of $a^0a^0c^+$. DFT+DMFT calculations show that the (avoided) band crossings due to octahedral tilting are shifted towards the Fermi level by correlations, hence making these points easier to reach experimentally. The DFT+DMFT calculations also suggest that octahedral tilting could stabilize further due to electron correlations. The energy gain due to tilting increased from $\sim$60 to 100 meV f.u.$^{-1}$ when going from DFT to DFT+DMFT. We note that the stabilization and description of octahedral rotations in $SrMoO_3$, which is a correlated metal, were recently addressed by Hampel and co-workers [44], where it was found that dynamic electronic correlations are important for obtaining the correct ground state. Furthermore, the Seebeck coefficient shows positive values slightly above the Fermi level for $a^0a^0c^-$ and $a^0a^0c^+$, as compared with the untilted $SrNbO_3$ that only displays negative values. Interestingly, the tilts are distinguishable due to the difference in the required chemical potential needed to observe positive values of the Seebeck coefficient. The peak in the optical loss function shows tunability with respect to octahedral tilting. Furthermore, the trends in peak position (and hence plasma frequency) and heights are different for the two tilts. We also show that the small feature around 2.75 eV is sensitive to octahedral tilting, which could explain the absence of this peak in experiments; see Ref. [14].

With the recent interest in $SrNbO_3$ we hope to give guidance for how the octahedral tilting behaves in the material but also suggest that tilting modes other than $a^0a^0c^-$ should be considered and investigated further in perovskite oxides. The pronounced features in thermoelectric and optical properties with respect to octahedral tilting could be used as an indication of tilting in $SrNbO_3$, and of the changes in the electronic structure therein.

TABLE I. Predicted lattice parameters using PBEsol in units of Å. In the strained cases, the relaxed out-of-plane parameter is presented.

Biaxial strain (%)	SrNbO₃	SrTiO₃
−3.0	4.095	3.974
−2.0	4.073	3.947
−1.0	4.047	3.922
−0.5	4.033	3.910
0.0	4.018	3.896
+0.5	4.007	3.887
+1.0	3.997	3.876
+2.0	3.979	3.855
+3.0	3.964	3.836

APPENDIX A: LATTICE PARAMETERS FOR A 5-ATOM CELL

The equilibrium lattice parameters were calculated for SrNbO₃ and SrTiO₃ with varying degrees of biaxial strain. This was done using the high-symmetry 5-atom unit cells. The objective is to find lattice parameters that can be used for all the following DFT calculations. For biaxial strain, the lattice parameters are given by $a = b = a_0(\epsilon + 1)$, where $a_0 = b_0$ is the relaxed unstrained lattice parameter and ϵ is the biaxial strain. The results are shown in Table I.

As expected, the lattice parameter of SrNbO₃ is substantially larger than that of SrTiO₃ [12]. Our predicted unstrained lattice parameters were 3.8958 and 4.0182 Å, which is in excellent agreement with the experimental values 3.905 and 4.023 Å for the titanate and niobate, respectively [12]. The difference between our predicted unstrained lattice parameter and the literature value is −0.009 and −0.005 Å for SrTiO₃ and SrNbO₃, respectively. In the following, the lattice parameters presented in Table I are kept fixed for a given strain value.

APPENDIX B: DRUDE TERM FOR INTRABAND TRANSITIONS

A phenomenological Drude intraband term was included in the calculation of the dielectric function:

$$\epsilon_{\text{intra}}(\omega) = \epsilon_{\text{intra}}^{(1)}(\omega) + i\epsilon_{\text{intra}}^{(2)}(\omega), \tag{B1}$$
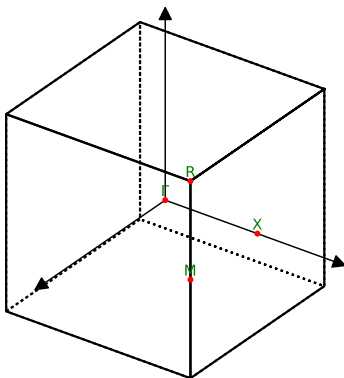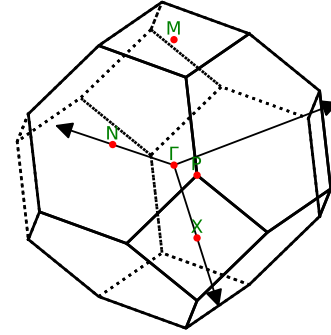

FIG. 7. BZ for $a^0a^0a^0$.

FIG. 8. BZ for $a^0a^0c^-$.

where the real and imaginary parts are given by

$$\epsilon_{\text{intra}}^{(1)}(\omega) = 1 - \frac{\omega_{p,\text{intra}}^2}{\omega^2 + \gamma^2}, \tag{B2}$$

$$\epsilon_{\text{intra}}^{(2)}(\omega) = \frac{\gamma\omega_{p,\text{intra}}^2}{\omega^3 + \omega\gamma^2}. \tag{B3}$$

Here $\omega_{p,\text{intra}}$ is the intraband plasma frequency [46] and $\gamma = 0.3$ eV is the inverse lifetime chosen in this work to reproduce the broadening in Ref. [18].

APPENDIX C: FIRST BRILLOUIN ZONE FOR DIFFERENT TILTS

In Figs. 7–9 the first Brillouin zones of $a^0a^0a^0$, $a^0a^0c^-$, and $a^0a^0c^+$ are shown. Note that the coordinate systems for the tilted structures are rotated 45° around the z-axis of the untilted structure.

APPENDIX D: STABILITY OF TILTS WITH CHARGE

The effect of electron (hole) doping on the tilting stability is presented in Fig. 10.
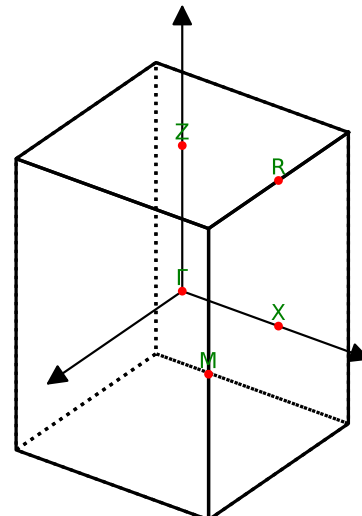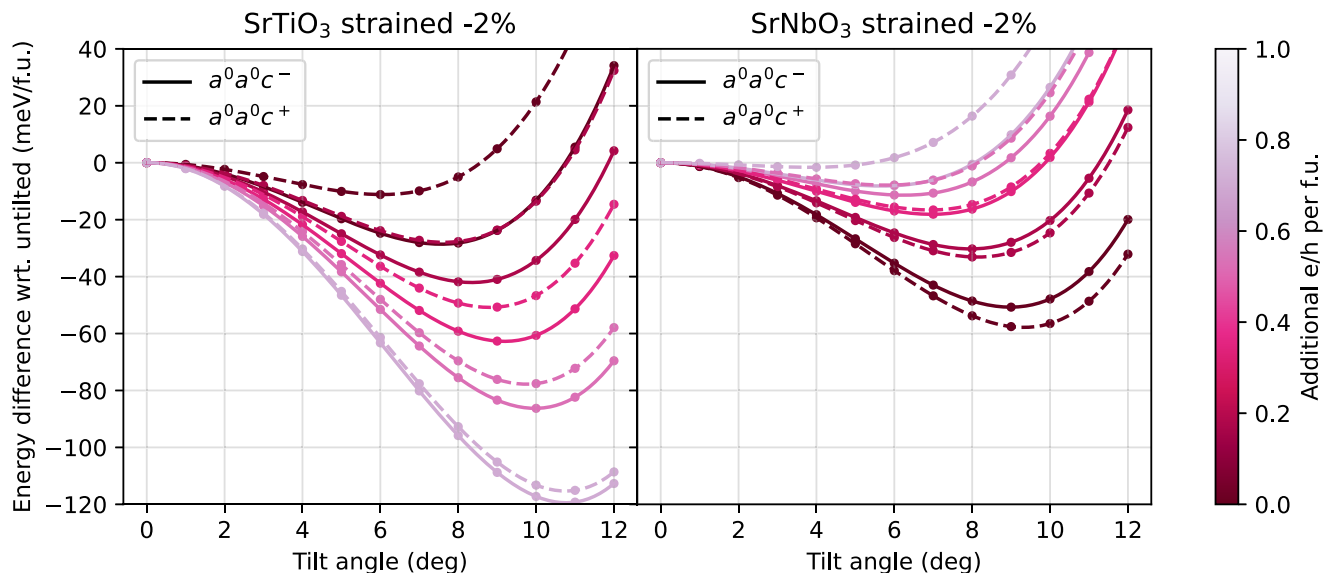

FIG. 9. BZ for $a^0a^0c^+$.

FIG. 10. Effect of electron (hole) doping on tilting stability of SrTiO$_3$ (SrNbO$_3$) under $-2°$ biaxial strain. SrTiO$_3$ to the left and SrNbO$_3$ to the right. The darkest purple lines correspond to undoped systems, and lighter lines correspond to more electrons (or holes). Adding electrons to SrTiO$_3$ causes the two tilt modes to stabilize. Furthermore, the addition of an electron reduces the difference in energy between *in-phase* and *out-of-phase* tilting. SrNbO$_3$ shows destabilization of tilts with the addition of holes. For SrNbO$_3$ there is a critical point at which the optimal tilt transitions from *in-phase* to *out-of-phase*.

APPENDIX E: t_{2g} SPLITTING MAP

A map of the t_{2g} splitting can be found in Fig. 11.

APPENDIX F: ALL OCTAHEDRAL TILTS

Figures 12 and 13 show the energy landscapes for the octahedral tilt modes in SrNbO$_3$ and SrTiO$_3$ over a wide range of strain values.
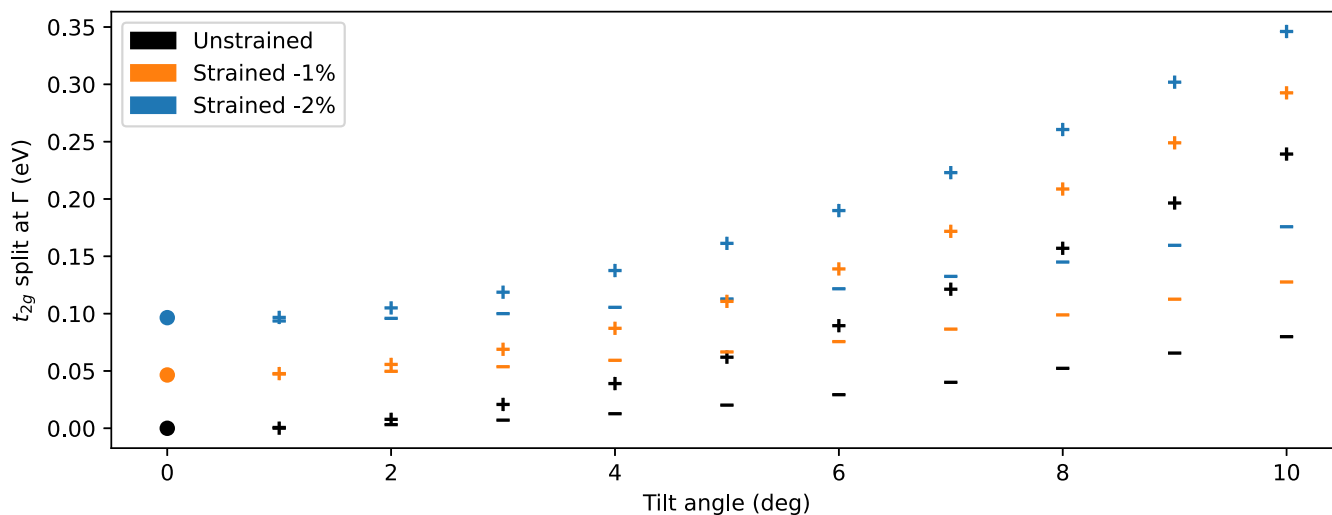

FIG. 11. Splitting between the t_{2g} orbitals at Γ. Circles denote untilted, plus signs denote $a^0a^0c^+$, and minus signs denote $a^0a^0c^-$.
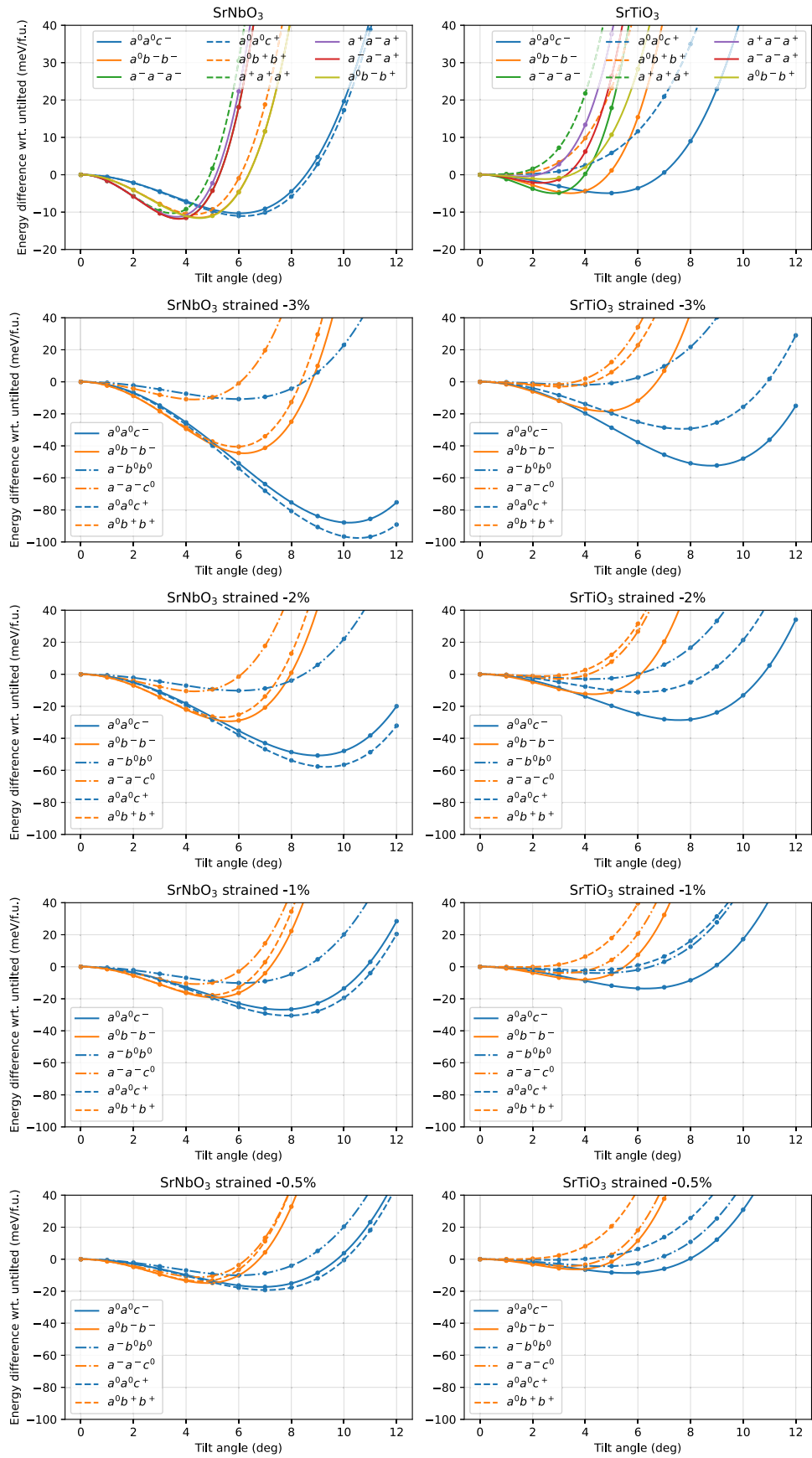
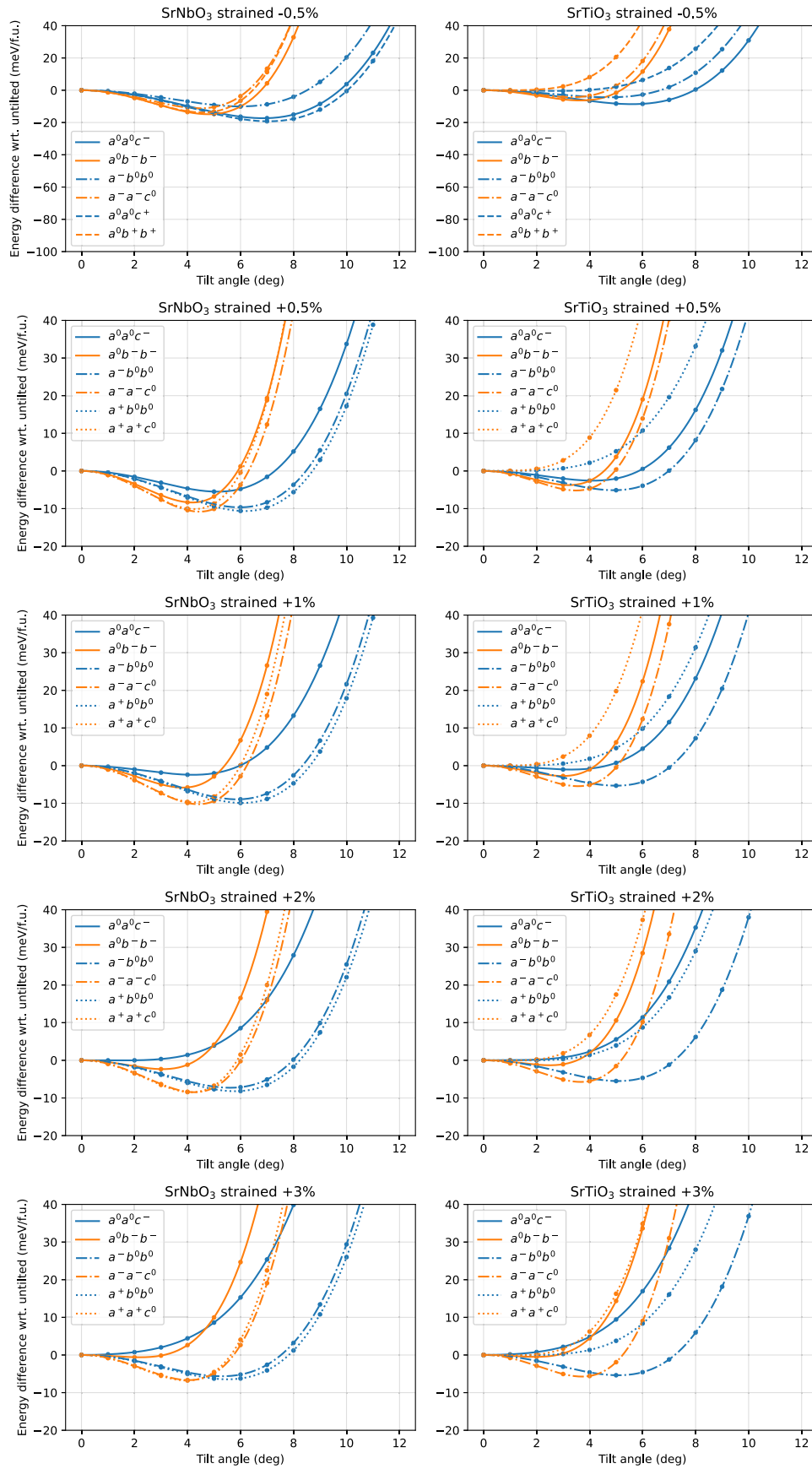FIG. 12. Octahedral tilting for SrNbO₃ and SrTiO₃ under various strains.

FIG. 13. Octahedral tilting for SrNbO$_3$ and SrTiO$_3$ under various strains.
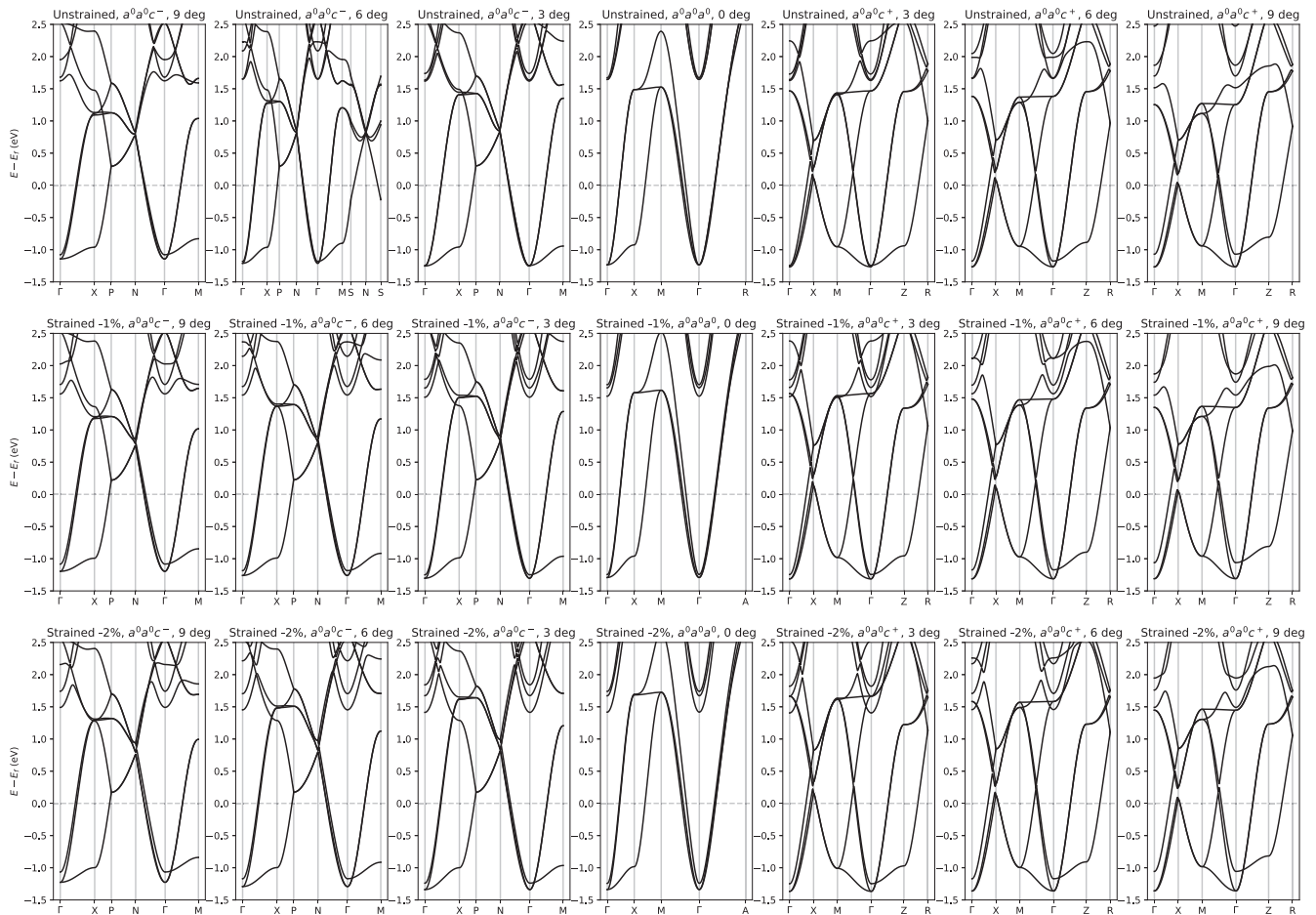
FIG. 14. Map of the band structure of $SrNbO_3$ for different tilt angles under compressive strain.

APPENDIX G: ALL BAND STRUCTURES

A map of the band structure of $SrNbO_3$ for various strains can be found in Fig. 14. Both in-phase and out-of-phase tilting modes are shown.

[1] A. S. Bhalla, R. Guo, and R. Roy, The perovskite structure - A review of its role in ceramic science and technology, Mater. Res. Innovations **4**, 3 (2000).

[2] P. K. Panda and B. Sahoo, PZT to lead free piezo ceramics: A review, Ferroelectrics **474**, 128 (2015).

[3] Y. Yin, B. Tudu, and A. Tiwari, Recent advances in oxide thermoelectric materials and modules, Vacuum **146**, 356 (2017).

[4] J. Sunarso, S. S. Hashim, N. Zhu, and W. Zhou, Perovskite oxides applications in high temperature oxygen separation, solid oxide fuel cell and membrane reactor: A review, Prog. Energy Combust. Sci. **61**, 57 (2017).

[5] J. F. Schooley, W. R. Hosler, and M. L. Cohen, Superconductivity in Semiconducting SrTiO₃, Phys. Rev. Lett. **12**, 474 (1964).

[6] M. Baldini, T. Muramatsu, M. Sherafati, H. Kwang Mao, L. Malavasi, P. Postorino, S. Satpathy, and V. V. Struzhkin, Origin of colossal magnetoresistance in LaMnO₃ manganite, Proc. Natl. Acad. Sci. USA **112**, 10869 (2015).

[7] F. J. Wong, S. H. Baek, R. V. Chopdekar, V. V. Mehta, H. W. Jang, C. B. Eom, and Y. Suzuki, Metallicity in LaTiO₃ thin films

induced by lattice deformation, Phys. Rev. B **81**, 161101(R) (2010).

[8] M. Gu, J. Laverock, B. Chen, K. E. Smith, S. A. Wolf, and J. Lu, Metal-insulator transition induced in CaVO₃ thin films, J. Appl. Phys. **113**, 133704 (2013).

[9] J. M. Ok, N. Mohanta, J. Zhang, S. Yoon, S. Okamoto, E. S. Choi, H. Zhou, M. Briggeman, P. Irvin, A. R. Lupini, Y. Y. Pai, E. Skoropata, C. Sohn, H. Li, H. Miao, B. Lawrie, W. S. Choi, G. Eres, J. Levy, and H. N. Lee, Correlated oxide Dirac semimetal in the extreme quantum limit, Sci. Adv. **7**, eabf9631 (2021).

[10] J. M. Rondinelli and N. A. Spaldin, Structure and properties of functional oxide thin films: Insights from electronic-structure calculations, Adv. Mater. **23**, 3363 (2011).

[11] J. M. Rondinelli, S. J. May, and J. W. Freeland, Control of octahedral connectivity in perovskite oxide heterostructures: An emerging route to multifunctional materials discovery, MRS Bull. **37**, 261 (2012).

[12] D. Oka, Y. Hirose, S. Nakao, T. Fukumura, and T. Hasegawa, Intrinsic high electrical conductivity of stoichiometric SrNbO$_3$ epitaxial thin films, Phys. Rev. B **92**, 205102 (2015).

[13] A. Paul and T. Birol, Strain tuning of plasma frequency in vanadate, niobate, and molybdate perovskite oxides, Phys. Rev. Mater. **3**, 085001 (2019).

[14] Y. Park, J. Roth, D. Oka, Y. Hirose, T. Hasegawa, A. Paul, A. Pogrebnyakov, V. Gopalan, T. Birol, and R. Engel-Herbert, SrNbO$_3$ as a transparent conductor in the visible and ultraviolet spectra, Commun. Phys. **3**, 102 (2020).

[15] X. G. Zhao, Z. Wang, O. I. Malyi, and A. Zunger, Effect of static local distortions vs. dynamic motions on the stability and band gaps of cubic oxide and halide perovskites, Mater. Today **49**, 107 (2021).

[16] J. Varignon, M. Bibes, and A. Zunger, Origin of band gaps in 3d perovskite oxides, Nat. Commun. **10**, 1658 (2019).

[17] N. Mott, *Metal-Insulator Transitions* (CRC, Boca Raton, FL, 2004).

[18] M. Mirjolet, M. Kataja, T. K. Hakala, P. Komissinskiy, L. Alff, G. Herranz, and J. Fontcuberta, Optical plasmon excitation in transparent conducting SrNbO$_3$ and SrVO$_3$ thin films, Adv. Opt. Mater. **9**, 2100520 (2021).

[19] W. Kohn and L. J. Sham, Self-consistent equations including exchange and correlation effects, Phys. Rev. **140**, A1133 (1965).

[20] P. E. Blöchl, Projector augmented-wave method, Phys. Rev. B **50**, 17953 (1994).

[21] G. Kresse and D. Joubert, From ultrasoft pseudopotentials to the projector augmented-wave method, Phys. Rev. B **59**, 1758 (1999).

[22] G. Kresse and J. Furthmüller, Efficient iterative schemes for ab initio total-energy calculations using a plane-wave basis set, Phys. Rev. B **54**, 11169 (1996).

[23] J. P. Perdew, A. Ruzsinszky, G. I. Csonka, O. A. Vydrov, G. E. Scuseria, L. A. Constantin, X. Zhou, and K. Burke, Restoring the Density-Gradient Expansion for Exchange in Solids and Surfaces, Phys. Rev. Lett. **100**, 136406 (2008).

[24] U. Aschauer and N. A. Spaldin, Competition and cooperation between antiferrodistortive and ferroelectric instabilities in the model perovskite SrTiO$_3$, J. Phys.: Condens. Matter **26**, 122203 (2014).

[25] A. Togo and I. Tanaka, spglib: A software library for crystal symmetry search, arXiv:1808.01590.

[26] K. Haule, C.-H. Yee, and K. Kim, Dynamical mean-field theory within the full-potential methods: Electronic structure of CeIrIn$_5$, CeCoIn$_5$, and CeRhIn$_5$, Phys. Rev. B **81**, 195107 (2010).

[27] J. P. Perdew, K. Burke, and M. Ernzerhof, Generalized Gradient Approximation Made Simple, Phys. Rev. Lett. **77**, 3865 (1996).

[28] P. Blaha, G. K. H. Madsen, D. Kvasnicka, and J. Luitz, *WIEN2K, An Augmented Plane Wave + Local Orbitals Program for Calculating Crystal Properties* (Karlheinz Schwarz, Techn. Universität Wien, Austria, 2001).

[29] K. Haule, Quantum monte carlo impurity solver for cluster dynamical mean-field theory and electronic structure calcula-

[30] G. K. Madsen, J. Carrete, and M. J. Verstraete, BoltzTraP2, a program for interpolating band structures and calculating semi-classical transport coefficients, Comput. Phys. Commun. **231**, 140 (2018).

[31] M. Gajdoš, K. Hummer, G. Kresse, J. Furthmüller, and F. Bechstedt, Linear optical properties in the projector-augmented wave methodology, Phys. Rev. B **73**, 045112 (2006).

[32] A. M. Glazer, The classification of tilted octahedra in perovskites, Acta Crystallogr. Sect. B **28**, 3384 (1972).

[33] H. Hannerz, G. Svensson, S. Y. Istomin, and O. G. D'Yachenko, Transmission Electron Microscopy and Neutron Powder Diffraction Studies of GdFeO$_3$ Type SrNbO$_3$, J. Solid State Chem. **147**, 421 (1999).

[34] J. Young and J. M. Rondinelli, Octahedral rotation preferences in perovskite iodides and bromides, J. Phys. Chem. Lett. **7**, 918 (2016).

[35] R. L. Johnson-Wilke, D. Marincel, S. Zhu, M. P. Warusawithana, A. Hatt, J. Sayre, K. T. Delaney, R. Engel-Herbert, C. M. Schlepütz, J. W. Kim, V. Gopalan, N. A. Spaldin, D. G. Schlom, P. J. Ryan, and S. Trolier-Mckinstry, Quantification of octahedral rotations in strained LaAlO$_3$ films via synchrotron x-ray diffraction, Phys. Rev. B **88**, 174101 (2013).

[36] M. Moreau, A. Marthinsen, S. M. Selbach, and T. Tybell, Strain-phonon coupling in (111)-oriented perovskite oxides, Phys. Rev. B **96**, 094109 (2017).

[37] F. Bruneval, C. Varvenne, J. P. Crocombette, and E. Clouet, Pressure, relaxation volume, and elastic interactions in charged simulation cells, Phys. Rev. B **91**, 024107 (2015).

[38] K. Uchida, S. Tsuneyuki, and T. Schimizu, First-principles calculations of carrier-doping effects in SrTiO$_3$, Phys. Rev. B **68**, 174107 (2003).

[39] V. M. Goldschmidt, Die Gesetze der Krystallochemie, Naturwissenschaften **14**, 477 (1926).

[40] N. Mohanta, J. M. Ok, J. Zhang, H. Miao, E. Dagotto, H. N. Lee, and S. Okamoto, Semi-Dirac and Weyl fermions in transition metal oxides, Phys. Rev. B **104**, 235121 (2021).

[41] D. M. Rowe, *CRC Handbook of Thermoelectrics* (CRC, Boca Raton, FL, 2018).

[42] P. Wei, W. Bao, Y. Pu, C. N. Lau, and J. Shi, Anomalous Thermoelectric Transport of Dirac Particles in Graphene, Phys. Rev. Lett. **102**, 166808 (2009).

[43] T. Zhu, P. E. Trevisanutto, T. C. Asmara, L. Xu, Y. P. Feng, and A. Rusydi, Generation of multiple plasmons in strontium niobates mediated by local field effects, Phys. Rev. B **98**, 235115 (2018).

[44] A. Hampel, J. Lee-Hand, A. Georges, and C. E. Dreyer, Correlation-induced octahedral rotations in SrMoO$_3$, Phys. Rev. B **104**, 035102 (2021).

[45] http://sdumont.lncc.br.

[46] J. Harl, G. Kresse, L. D. Sun, M. Hohage, and P. Zeppenfeld, Ab initio reflectance difference spectra of the bare and adsorbate covered Cu(110) surfaces, Phys. Rev. B **76**, 035436 (2007).